

Characterizing the impact of the magnetic field in the frequency domain for a multiwave atom interferometer

Xudong Ren,¹ Wenhua Yan,^{1,*} Yukun Yang,¹ Xiaobing Deng,¹ Wenjie Xu,¹ Zhongkun Hu,^{1,2} and Minkang Zhou^{1,†}

¹MOE Key Laboratory of Fundamental Physical Quantities Measurement, Hubei Key Laboratory of Gravitation and Quantum Physics, PGMF and School of Physics, Huazhong University of Science and Technology, Wuhan 430074, People's Republic of China

²Wuhan Institute of Quantum Technology, Wuhan 430206, People's Republic of China



(Received 13 July 2023; revised 19 October 2023; accepted 21 November 2023; published 11 December 2023)

We implement a magnetic-field-sensitive multiwave atom Ramsey interferometer based on radio-frequency (RF) field-coupled Zeeman states, and we theoretically derive and experimentally measure its frequency-domain transfer function with low-pass filtering characteristics. In addition, we investigate a potential application scheme of the transfer functions for interference fringe recovery. As the measurements involve the ac magnetic field, a Raman spectrum-based solution is implemented to calibrate the actual ac magnetic field amplitude at the position of the atom inside the vacuum chamber. The methods demonstrated in this work will help to improve the performance of the atom interferometer and are also useful in Ramsey interference-based systems and spinor Bose-Einstein condensates (BEC) experiments.

DOI: [10.1103/PhysRevA.108.063309](https://doi.org/10.1103/PhysRevA.108.063309)

I. INTRODUCTION

The cold-atom interferometer has a wide range of applications in various fields, such as inertial sensing [1–5], the measurement of fundamental physical constants [6–9], precision frequency measurements [10,11], precision magnetic-field sensing [3,12,13], the study of the fundamental properties of quantum mechanics [14], and tests of fundamental physical laws [15–17]. In particular, the multiwave atom interferometer [18,19] can increase the sensitivity (and thus resolution) of the interferometer through increased fringe slopes [19–21]. Such an interferometer has been recently proposed and demonstrated using atomic external momentum states [22,23] or internal spin states [13,20,21].

Among them, in the atomic systems with spin degrees of freedom, it is not only possible to utilize the spin states to implement multiwave interferometers that do not rely on spatially separated paths [13,20], but also to utilize the spin state to implement many types of atom interferometer-based high-precision magnetic-field sensing [11–13,24,25]. However, in such systems, magnetic fields inherently cause significant impacts, inducing noise [26,27], thus causing the decoherence of the quantum states and limiting the system coherence time. In addition, precise characterization of the magnetic field is crucial for the effective manipulation of quantum states in many experiments utilizing atomic systems with spin degrees of freedom, such as spin-dependent optical lattices [28–30], many-body entanglement states generation [31–33], and precision measurements based on atom interferometers [2,3,7,9–11,17].

Therefore, the characterization of the response of such systems to magnetic fields is important. Measurement of the transfer function in the frequency domain provides us with a solution. Based on the transfer function, on the one hand, we can characterize the impact of the magnetic field on the systems, and on the other hand, we can acquire valuable information in a magnetically noisy environment. The merit of this is that such systems provide a promising experimental platform, that is, the construction of a multiwave atom interferometer utilizing spin states to study the response of the systems to the magnetic field.

In this work, we implement a magnetically sensitive multiwave atom Ramsey interferometer based on radio-frequency (RF) field-coupled Zeeman states in an unshielded, titanium vacuum chamber. We theoretically derive and experimentally measure the transfer function of the interferometer to magnetic fields. In addition, we investigate the application of transfer functions in an artificial magnetically noisy environment and provide a feasible scheme for interference fringe recovery. These methods could be beneficial for *in situ* corrections of errors introduced by magnetic field for precision atom interferometers, and will also be useful for some other Ramsey interference-based systems (such as atomic clocks [10,11], trapped-ion systems [34,35], nitrogen-vacancy (N-V) centers in diamonds [36,37]) and some spinor Bose-Einstein condensates (BEC) experiments [28–33], which are impacted by the magnetic field.

This article is organized as follows. We present the basic theory and experimental setup in Secs. II and III. The experimental results related to the magnetic-field response of the interferometer and the application of the transfer function are demonstrated in detail in Sec. IV. In Sec. V, we conclude this work with a summary.

*yanwenhua@hust.edu.cn

†zmk@hust.edu.cn

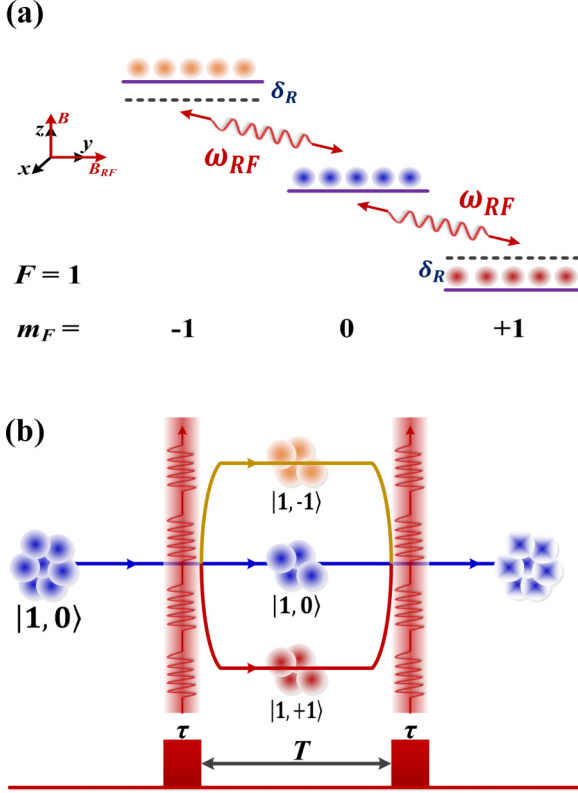


FIG. 1. (a) Level scheme for RF coupling. The bias magnetic field along the z axis induces Zeeman states and the RF field transports along the y axis to realize the state coupling. (b) Time sequence of the multiwave atom interferometer. Two RF pulses of duration τ are illuminating atoms with a time interval T to implement Ramsey-type interference.

II. THEORY

A. Multiwave Ramsey interference

We begin with the analysis of our atom interferometer where the cold ^{87}Rb atom ensemble is in the $5^2S_{1/2}|F=1\rangle$ manifold shown in Fig. 1(a).

The homogeneous bias magnetic field $\mathbf{B} = B_z \mathbf{e}_z$ along the z axis is applied to define the quantization axis. In this field, Zeeman states have different energies, considering the first-order Zeeman effect, which is given by $H_0 = -\boldsymbol{\mu} \cdot \mathbf{B}$, where $\boldsymbol{\mu}$ is the atomic magnetic dipole moment operator. Based on the similar theoretical framework in Ref. [38], we use the RF field $\mathbf{B}_{\text{RF}} = B_{\text{RF}} \mathbf{e}_y \cos(\omega_{\text{RF}} t + \varphi_{\text{RF}})$ to couple the Zeeman states, where the RF field is along the y axis with an amplitude of B_{RF} , a frequency ω_{RF} , and an initial phase φ_{RF} . The atom-field interactions can be expressed as $H_{\text{int}} = -\boldsymbol{\mu} \cdot \mathbf{B}_{\text{RF}}$, and the total system Hamiltonian is given by $H = H_0 + H_{\text{int}}$, the evolution of the system depends on the Schrödinger equation

$$i\hbar \frac{\partial}{\partial t} |\psi(t)\rangle = H |\psi(t)\rangle, \quad (1)$$

where $|\psi(t)\rangle = [C_{-1}(t), C_0(t), C_{+1}(t)]^T$ is the Zeeman state vector of the $F=1$ spin system. Within the rotating-wave-

approximation (RWA), the Hamiltonian is given by [39]

$$H_R = \hbar \begin{pmatrix} -\delta_R & \sqrt{2}\Omega e^{i\varphi_{\text{RF}}} & 0 \\ \sqrt{2}\Omega e^{-i\varphi_{\text{RF}}} & 0 & \sqrt{2}\Omega e^{i\varphi_{\text{RF}}} \\ 0 & \sqrt{2}\Omega e^{-i\varphi_{\text{RF}}} & \delta_R \end{pmatrix}, \quad (2)$$

where the detuning $\delta_R = \omega_{\text{RF}} - k|\mathbf{B}|$, $k = \mu_B/2\hbar$, μ_B is the Bohr magneton, and Ω is the Rabi frequency to quantify the RF coupling strength. The effective Rabi frequency of RF coupling is given by $\Omega_{\text{eff}} = \sqrt{\delta_R^2 + (2\Omega)^2}$.

The final state $|\psi(t)\rangle$ after the single RF pulse can be written as

$$|\psi(t)\rangle = \mathbf{U}_R(t) |\psi(0)\rangle, \quad (3)$$

where $|\psi(0)\rangle$ is the wave function of the initial state and $\mathbf{U}_R(t)$ is the time evolution operator of this system [39].

A typical Ramsey interference sequence [40] is illustrated in Fig. 1(b). The final state of the interferometer can be expressed as

$$|\psi(\tau + T + \tau)\rangle = \mathbf{U}_R(\tau) \mathbf{U}_F(T) \mathbf{U}_R(\tau) |\psi(0)\rangle, \quad (4)$$

where the free evolution operator $\mathbf{U}_F(T)$ is diagonal, with elements $e^{-i\delta_{R,ii}T}$, where $\delta_{R,ii}$ is the diagonal element of H_R [39].

In particular, when atoms are in an initial state $|m_F=0\rangle$, and if we choose the parameter $2\Omega_{\text{eff}}\tau = \pi$, which is similar to the so-called π pulse in a two-level system [21], according to Eq. (4), the interferometer fringe behavior on state $|m_F=0\rangle$ is expressed as

$$P_\pi = \frac{1}{2} \{1 + \cos[2(\Delta\Phi_B)]\}, \quad (5)$$

where the interferometer phase shift $\Delta\Phi_B = \delta_R T$. This means that our multiwave atom interferometer is sensitive to magnetic field.

B. Transfer function of interferometer

By establishing the transfer function of the interferometer, we can quantitatively describe its sensitivity to the magnetic field. We first derive the sensitivity function of the interferometer to the magnetic field in the time domain, and from this, we derive the transfer function in the frequency domain.

In the time domain, the sensitivity function is a natural tool to characterize the influence of external fluctuations on the interferometer phase shift $\Delta\Phi_B$, such as the RF field phase φ_{RF} fluctuation. The interferometer sensitivity function is written as [41,42]

$$g_\varphi(t) = \lim_{\delta\varphi_{\text{RF}} \rightarrow 0} \frac{\delta\Phi_B(\delta\varphi_{\text{RF}}, t)}{\delta\varphi_{\text{RF}}}. \quad (6)$$

Following the similar derivation method in Ref. [41], we can get the $g_\varphi(t)$ in the multiwave Ramsey interference sequence whose expression is given by

$$g_\varphi(t) = \begin{cases} 2 \sin \left[\Omega_{\text{eff}} \left(t + \frac{T}{2} + \tau \right) \right], & -\frac{T}{2} - \tau \leq t < -\frac{T}{2}, \\ 2, & -\frac{T}{2} \leq t \leq \frac{T}{2}, \\ 2 \sin \left[\Omega_{\text{eff}} \left(\frac{T}{2} + \tau - t \right) \right], & \frac{T}{2} < t \leq \frac{T}{2} + \tau. \end{cases} \quad (7)$$

The resolving interferometric phase variation $\delta\Phi_B$ induced by the RF phase fluctuations, $\delta\varphi_{\text{RF}}$ can be written as

$$\delta\Phi_B = \int_{-\tau-T/2}^{\tau+T/2} g_\varphi(t) d\varphi_{\text{RF}} = \int_{-\tau-T/2}^{\tau+T/2} g_\varphi(t) \frac{d\varphi_{\text{RF}}}{dt} dt. \quad (8)$$

In another aspect, the total phase shift $\Delta\Phi_B$ is the sum of the phase difference on the interference path during the free evolution and the RF phase changes due to the atom-field interactions. That is, the free evolution phase accumulation caused by the atomic energy level shift can be equally regarded as the phase shift caused by the RF phase fluctuations. Therefore, considering the magnetic field fluctuations, this effect is shown by

$$\frac{d\varphi_{\text{RF}}}{dt} = k\delta B. \quad (9)$$

Thus, the phase variation due to the magnetic field fluctuations is expressed according to Eq. (8) as

$$\delta\Phi_B = \int_{-\tau-T/2}^{\tau+T/2} g_\varphi(t) (k\delta B) dt. \quad (10)$$

Following Eq. (6), the sensitivity function to the magnetic field can be written as [43]

$$g_B(t) = \lim_{\delta B \rightarrow 0} \frac{\delta\Phi_B(\delta B, t)}{\delta B} = k \int_t^{\tau+T/2} g_\varphi(t') dt'. \quad (11)$$

In the frequency domain, we can obtain the following results by applying the Laplace transform to Eq. (11):

$$|H_B(\omega)|^2 = \frac{k^2}{\omega^2} |H_{\varphi_{\text{RF}}}(\omega)|^2, \quad (12)$$

where $H_B(\omega)$ is the transfer function to the magnetic field, $H_{\varphi_{\text{RF}}}(\omega)$ is the transfer function to the RF phase. In detail, $|H_{\varphi_{\text{RF}}}(\omega)|^2 = |\omega G_{\varphi_{\text{RF}}}(\omega)|^2$, where $G_{\varphi_{\text{RF}}}(\omega)$ is the Fourier transform of the sensitivity function $g_\varphi(t)$. Based on the above results, we derive the transfer function $H_B(\omega)$ of the multiwave Ramsey interferometer as follows:

$$|H_B(\omega)|^2 = \frac{16\Omega_{\text{eff}}^2 k^2 (\omega \cos[(\frac{T}{2} + \tau)\omega] + \Omega_{\text{eff}} \sin[\frac{\omega T}{2}])^2}{\omega^2 (\omega^2 - \Omega_{\text{eff}}^2)^2}. \quad (13)$$

This is consistent with the so-called filter function derived based on dynamic decoupling theory [24,44], which differs only in the coefficients because of the multiwave interference. In other words, our procedure for deriving the transfer function can be generalized to arbitrary Ramsey-type interference. In this paper, we experimentally measure $|H_B(\omega)|^2$, as a way to characterize the transfer function $H_B(\omega)$.

The effect of magnetic-field fluctuations on the interferometer phase uncertainty σ_{Φ_B} can be expressed as [41]

$$\sigma_{\Phi_B}^2 = \int_0^{+\infty} |H_B(\omega)|^2 S_B(\omega) d\omega, \quad (14)$$

where $S_B(\omega)$ is the power spectral density of the magnetic field.

III. EXPERIMENTAL SETUP

Our experiments are carried out in an atom interferometer apparatus based on ultracold ensembles [45]. The

schematic of our physical system is shown in Fig. 2(a), where the two-dimensional magneto-optical trap (2D-MOT) and the three-dimensional magneto-optical trap (3D-MOT) are used to precool the atoms. One set of coils is placed close to the side of 3D-MOT and is driven by a waveform generator (KEYSIGHT 33600A) to generate an RF field along the y direction. The coil's diameter is about 30 mm. Another set of coils is placed above the 3D-MOT and driven by another same-type waveform generator to generate additional magnetic field modulations along the quantization axis (z direction). The bias magnetic field $\mathbf{B} = B_z \mathbf{e}_z$ is generated by the three-axis Helmholtz coils system, for which the high-precision source meters (KEITHLEY 2450) are used as the current source for this system. Using the Raman spectrum method [46], which is based on the stimulated Raman process to measure the magnetic field by the frequency spacing of the transition peaks, the strength of the bias field B_z is found to be 63.50 mG. According to the relation $\omega_{\text{RF}} = kB_z$, we set the driving frequency of the RF field to 44.45 kHz.

The time sequence used in our experiment is shown in Fig. 2(b). The cold ^{87}Rb atoms are prepared in the optical crossed dipole trap (OCDT) with double reservoirs and a dimple configuration. In combination with an optical pumping process and reasonable control of the evaporative cooling parameters, typically, about 3×10^5 atoms remain in the $|F=1\rangle$ manifold with a temperature of about 500 nK. About 75% of these are in the $|F=1, m_F=0\rangle$ state [47]. Then, the atoms are released from OCDT, subsequently, the multiwave Ramsey interference sequence (π - T - π) is applied to atoms. Before the atoms fly out of the ultracold atoms' preparation region, a Doppler-insensitive Raman pulse transfers the atoms from $|F=1, m_F=0\rangle$ state to $|F=2, m_F=0\rangle$ state. The atoms then reach the detection region, and the standard two-state sequential detection [1] is performed to deduce the transition probability [48]. The multiwave Ramsey fringes can be obtained by adjusting the RF frequency ω_{RF} during the free evolution step. One total experimental sequence takes 4.11 s.

IV. MEASUREMENT AND APPLICATION OF THE TRANSFER FUNCTION

We measure the transfer function $H_B(\omega)$ using the experimental procedure shown in Fig. 3. To measure the transfer function, a magnetic field modulation $B_m \sin(2\pi f_m t + \varphi_m)$ generated by the modulation coils is applied on the atoms. After the interference process, the interferometric phase variations are recorded as a function of f_m , and then we extract $|H_B(\omega)|^2$. However, these measurements involving ac magnetic field are carried out inside the titanium vacuum chamber. Therefore, to derive the transfer function, it is a prerequisite to calibrate the modulation field at the position of the atom. Finally, as a further validation and application of multiwave interferometer response to the magnetic field, we prove, in principle, a fringe recovery scheme based on the transfer function in an artificial magnetically noisy environment. Briefly, the experimental characterization of the multiwave interferometer response to the magnetic field consists of four parts: the measurement of the actual modulation field felt by the atom inside the chamber, the implementation of a magnetically sensitive multiwave interferometer,

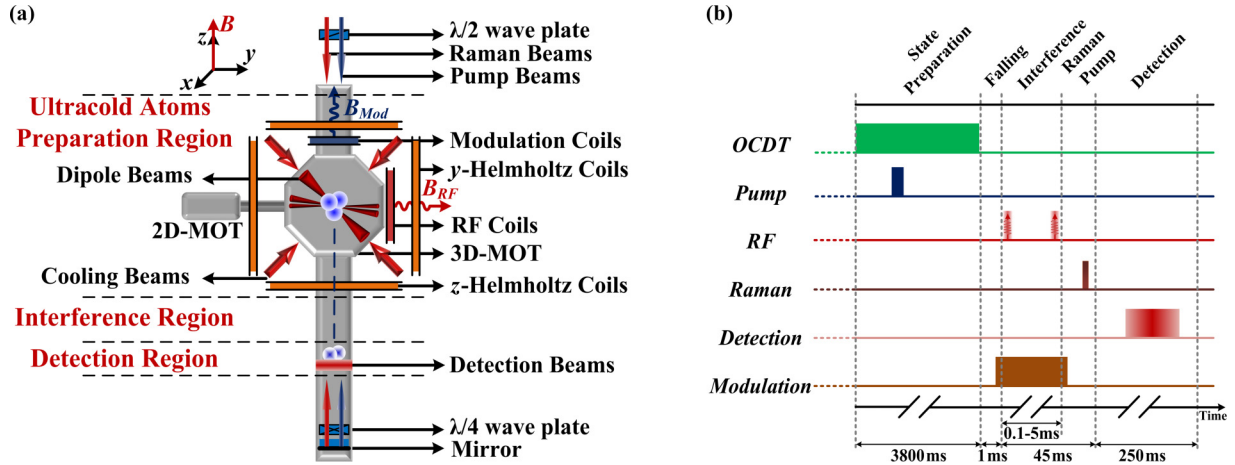


FIG. 2. Schematic of the experimental apparatus and the time sequence. (a) Atom interferometer physical system. The RF coils are used to generate the RF field, the modulation coils are used for magnetic field modulation, and the three-axis Helmholtz coils system (the x coils are not shown in the figure) is used to generate the bias magnetic field. And the cold atoms are prepared in the OCOT. (b) Experimental time sequence for multiwave atom interferometer.

the measurement of the transfer function, and the investigation of potential practical applications of the transfer function.

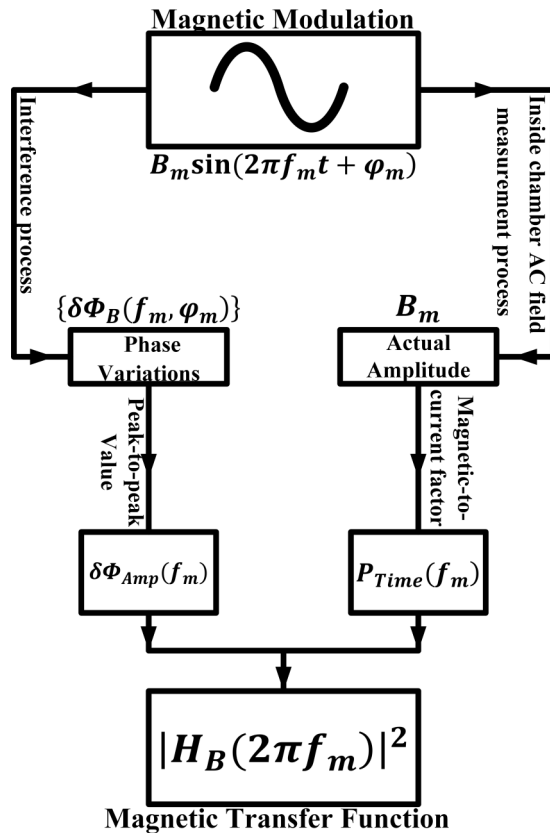


FIG. 3. Experimental procedure for measuring the transfer function $H_B(\omega)$ of the interferometer. The procedure consists of two aspects: on the one hand the phase variations $\delta\Phi_{Amp}(f_m)$ need to be recorded by the interference process under the effect of modulation field, on the other hand, the power $P_{Time}(f_m)$ need to be recorded by measuring the modulation field actually felt by the atom inside the vacuum chamber.

A. Measurement of ac magnetic field inside the vacuum chamber

In our atom interferometer, the characterization of the magnetic-field response involves an ac magnetic-field measurement inside the chamber. However, it is limited by the system, i.e., the ac magnetic field felt by the atom inside the chamber is difficult to be measured by placing magnetic sensors, so it is necessary to develop a method based on the atom itself that can measure the ac magnetic field inside the vacuum chamber at the position of the atom. The implementation scheme is shown in Fig. 4.

The modulation $B_m \sin(2\pi f_m t + \varphi_m)$ is applied to atoms. To measure the ac magnetic field amplitude B_m , the Raman spectrum method is applied under the modulation field. The Raman pulse in the experiment is less than $50 \mu\text{s}$ and the shortest modulation waveform period is at least ms level ($\sim 1 \text{ kHz}$). Therefore, the modulation waveform is slowly varying compared to the Raman pulse. At a fixed position applying the Raman pulse, we modulate the phase of the waveform to realize the shift of the ac magnetic field waveform in time, which is given by

$$B_{\text{mod}} = B_m \sin[2\pi f_m(t + t_M) + \varphi_m], \quad (15)$$

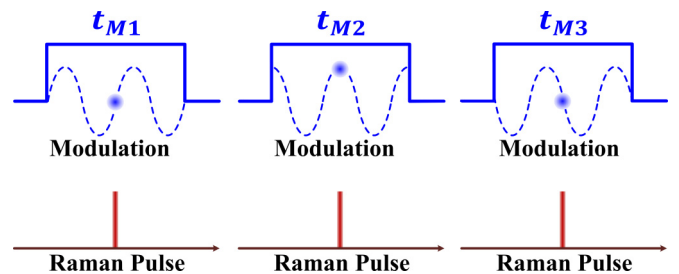


FIG. 4. The implementation scheme of the ac magnetic-field measurement inside the vacuum chamber. We scan the waveform of the modulation field with a short Raman pulse, converting the ac field measurement into the dc field measurement.

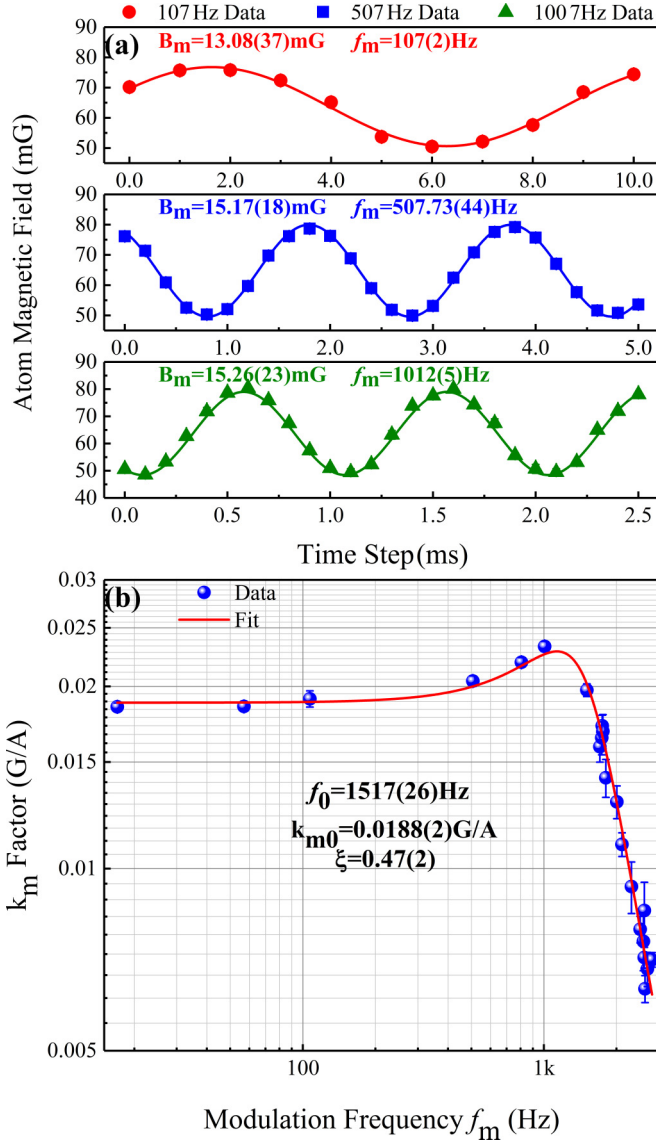


FIG. 5. The Results of the ac magnetic field measurement inside the vacuum chamber. (a) Typical ac field measurements. The solid lines are fitting using Eq. (15). (b) The factor k_m wide-band measurement results. The blue dots are experimental data, the red line is the fitting result.

where t_M is a suitable time step to implement waveform scanning. Figure 5(a) illustrates the measurements, where the fitted curves are given by Eq. (15). Even at kHz frequencies, data with enough time steps are acquired to make sure that the slow variation of the modulation field is captured. The results show that we implement the measurement of the ac magnetic field inside the titanium vacuum chamber and its oscillation frequency agrees with the modulation frequency f_m .

Furthermore, we repeat the above experimental procedure in a wider frequency range, and we define a factor k_m , which characterizes the ratio of the amplitude of the magnetic field B_m inside the chamber to the amplitude of the current I_m in the modulation coils. The factor k_m is recorded as a function of f_m and the results are shown with blue dots in Fig. 5(b). In addition, it can be seen that our results are in agreement with

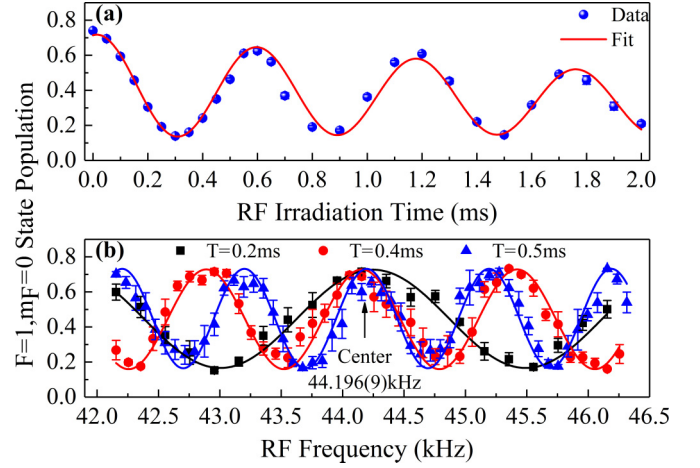


FIG. 6. (a) Rabi oscillation of $F = 1$ spin system. (b) Typical multiwave Ramsey interference fringes for magnetic-field measurement. Each plotted point represents the average over ten measurements. Error bars are statistical errors. The solid lines are fit using Eq. (5).

the conventional second-order low-pass filter model, which is given by

$$k_m = \frac{k_{m0}}{\sqrt{[1 - (\frac{f_m}{f_0})^2]^2 + 4\xi^2(\frac{f_m}{f_0})^2}}, \quad (16)$$

where k_{m0} is known as the system static sensitivity, f_0 is the natural frequency of the system, and ξ is the damping ratio [49]. From Fig. 5(b), the equivalent 3-dB bandwidth of our system for the ac magnetic field is about 2 kHz. This second-order low-pass filter characteristics may be due to the system consisting of the modulation coils and the titanium vacuum chamber, which hinders the propagation of the ac magnetic field.

B. Implementation of magnetically sensitive multiwave interferometer

To realize the RF-coupled multiwave Ramsey interference, we need to first determine the duration of the RF π pulse according to $2\Omega_{\text{eff}}\tau = \pi$. Rabi oscillation is implemented by varying the irradiation duration of a single RF pulse. As shown in Fig. 6(a), the duration of the RF π pulse is 290 μ s, and the RF excitation efficiency can reach more than 60%. We adjust the RF frequency ω_{RF} from shot to shot to obtain interference fringes, as shown in Fig. 6(b).

It is clear that the fringe pattern for multiwave Ramsey interference shows good qualitative agreement with Eq. (5). According to the fringe center 44.196(9) kHz, the absolute magnetic field value of $B_z = 63.137(13)$ mG can be deduced according to $\delta_R = \omega_{\text{RF}} - kB_z$. Meanwhile, the fringe contrast of about 60% is limited by the impurity of the initial state [47] and the small shifts of the overlapped fringe centers under different evolution times T indicate T -dependant systematic error(s) to be evaluated.

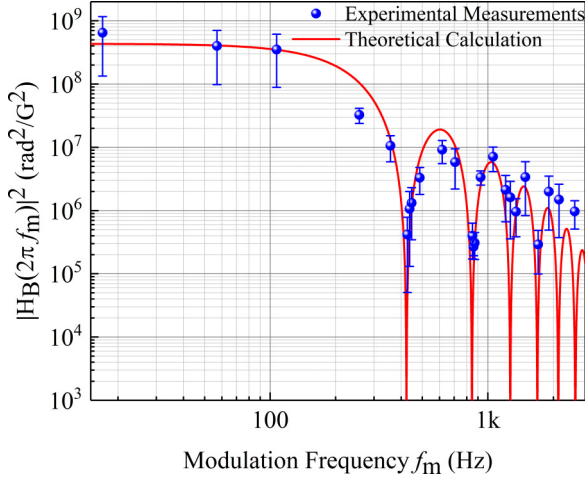


FIG. 7. The result of the transfer function $H_B(\omega)$ measurement with parameters $T = 2$ ms and $\tau = 0.29$ ms. The theoretical calculation is displayed in the red line and the experimental results are shown as blue dots.

C. Result for the measurement of the transfer function

In the frequency domain, the transfer function can be extracted from Eq. (14). When the magnetic field fluctuation is a known regular sinusoidal modulation, $B_m \sin(2\pi f_m t + \varphi_m)$, the response of the interferometer to it should be the phase variation $\delta\Phi_B(f_m, \varphi_m)$, related to the initial phase of the modulation field φ_m at a given modulation frequency f_m . In this case, Eq. (14) can be simplified as

$$\delta\Phi_B^2(f_m, \varphi_m) = 2\pi |H_B(2\pi f_m)|^2 S_B(f_m) \Delta f_m. \quad (17)$$

On the one hand, according to the energy conservation, the power of the modulation field can be expressed as $P_{\text{Time}}(f_m) = S_B(f_m) \Delta f_m$. On the other hand, to eliminate the effect of φ_m in the experiment, we repeat the measurements in a series of φ_m , for example, $\{\varphi_m\} = \{0, 90, 180, 270, 360\}^\circ$. Then the phase variations will be $\{\delta\Phi_B(f_m, \varphi_m)\} = \{\delta\Phi_0, \delta\Phi_{90}, \delta\Phi_{180}, \delta\Phi_{270}, \delta\Phi_{360}\}$. To obtain half of the peak-to-peak values $\delta\Phi_{\text{Amp}}(f_m)$ in this series of phase variations, the effect of φ_m can be eliminated [43]. In the end, based on the power of a sinusoidal signal and the factor k_m , we measure the transfer function using the following relationship:

$$|H_B(2\pi f_m)|^2 = \frac{\delta\Phi_{\text{Amp}}^2(f_m)}{2\pi P_{\text{Time}}(f_m)} = \frac{\delta\Phi_{\text{Amp}}^2(f_m)}{2\pi \left(\frac{k_m I_m}{\sqrt{2}}\right)^2}. \quad (18)$$

So, we need to record the $\delta\Phi_{\text{Amp}}(f_m)$ and the current amplitude I_m in the modulation coils as a function of f_m , and find the correlation factor k_m from our ac magnetic-field experimental results. We can then calculate the transfer function $|H_B(2\pi f_m)|^2$. The results, which are displayed in Fig. 7, together with the theoretical values calculated by Eq. (13) in parameters $T = 2$ ms and $\tau = 0.29$ ms, clearly demonstrate the oscillatory behavior and the low-pass filtering characteristics of the transfer function. The experimental results show that our interferometer is sensitive to magnetic fields at low frequencies. The vertical error bars in our results show the statistical error, which mainly comes from the significant

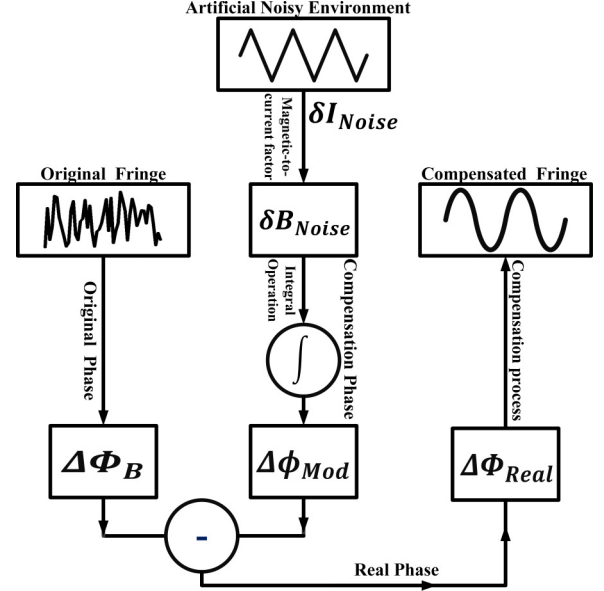


FIG. 8. Experimental protocol for the fringe recovery scheme. The artificial noise current is acquired by a data acquisition unit, the noise compensation phase is obtained based on the transfer function and subtracting the compensation phase from the original phase to obtain the real phase.

uncertainty in the measurement of $\delta\Phi_{\text{Amp}}(f_m)$, since our system is unshielded and subject to magnetic field noise.

D. Application of the transfer function

The transfer function $H_B(\omega)$, as a fundamental characteristic of the multiwave interferometer, frames a link between the magnetic field and the interferometer phase shift in the frequency domain, and its general application is to calculate the phase noise induced by external magnetic field fluctuations according to Eq. (14), which is commonly used to evaluate the influence on atom interferometer resolution [42]. Furthermore, we consider an application scene where the atom interferometer is perturbed by an artificial magnetically noisy environment, which is made by magnetic field white noise in the direction of the quantization axis. Similarly, the phase noise induced by the artificial white noise can be evaluated with Eq. (14), but if there is a feasible mechanism to compensate for such phase noise, it implies that the atom interferometer will be able to acquire effective information in such a noisy environment, which thus broadens the range of applications of the transfer function and it can potentially enhance the environmental adaptability of the atom interferometer.

For the motivation mentioned above, we investigate and prove, in principle, a transfer function-based interference fringe recovery scheme in an artificial magnetically noisy environment, and its implementation protocol is illustrated in Fig. 8. To simulate such a noisy environment, we utilize the modulation coils to generate white-noise-type current modulation δI_{Noise} to worsen the magnetic-field environment felt by atoms. In addition, we reduce the free evolution time T to 0.2 ms or 0.4 ms to ensure that we can still acquire

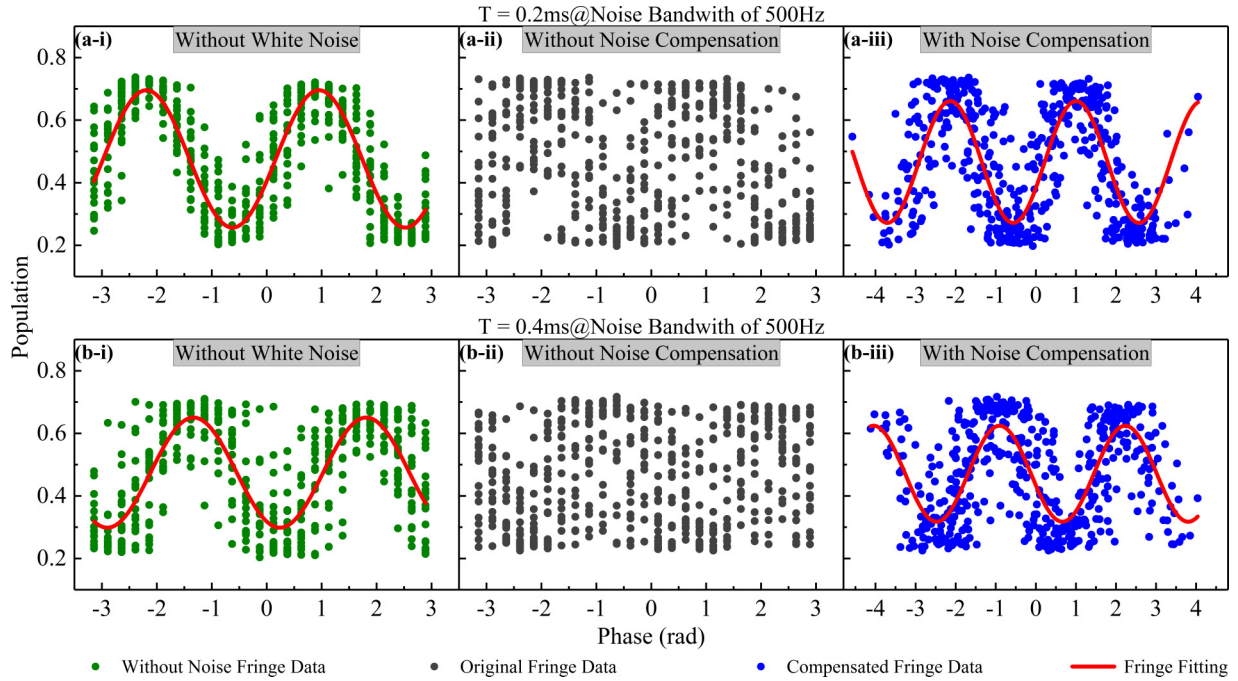


FIG. 9. Experimental demonstration results for the fringe recovery scheme. (a-i, ii, iii) $T = 0.2$ ms results. (b-i, ii, iii) $T = 0.4$ ms results. The green dots in (a-i) and (b-i) indicate the data without artificial white noise. The black dots in (a-ii) and (b-ii) indicate the data without the noise compensation and the blue dots in (a-iii) and (b-iii) indicate the data with the noise compensation. In total, there are 20 fringes and 25 data points per fringe, respectively. The red lines are the fitting results.

interference fringes with a reasonable contrast in this magnetically noisy environment. Similar to the vibrational noise compensation scheme in atomic interference gravimetry [42], when the multiwave atom interferometer is in this magnetically noisy environment, the real phase shift should be expressed as

$$\Delta\Phi_{\text{Real}} + \Delta\phi_{\text{others}} = \Delta\Phi_B - \Delta\phi_{\text{Mod}}, \quad (19)$$

where $\Delta\phi_{\text{Mod}}$ is the phase noise introduced by the artificial magnetically noisy environment, and $\Delta\phi_{\text{others}}$ is the sum of the phase noises contribution by other noise sources, which includes the original magnetic field noise in our system. The goal is to verify whether the multiwave interferometer can compensate the phase noise $\Delta\phi_{\text{Mod}}$ from the original phase shift $\Delta\Phi_B$, so as to demonstrate the practicability of the scheme that we propose. This can be implemented using the time domain model Eq. (10) of the transfer function. Thus, $\Delta\phi_{\text{Mod}}$ can be obtained according to the following relationship:

$$\Delta\phi_{\text{Mod}} = \int_{-\tau-T/2}^{\tau+T/2} g_{\varphi}(t)[k\delta B_{\text{Noise}}]dt, \quad (20)$$

where δB_{Noise} is the artificial white-noise magnetic field felt by the atoms, depending on the modulation current δI_{Noise} and the factor k_m . The detected phase noise $\Delta\phi_{\text{Mod}}$ is subtracted from the original phase shift $\Delta\Phi_B$ to obtain the corrected phase shift $\Delta\Phi_{\text{Real}}$. In this way, the interference fringe is recovered.

Since our multiwave interferometer is sensitive to low-frequency magnetic fields, a reasonable bandwidth of magnetic-field modulation can amplify the effect of noise. We choose 500-Hz bandwidth white noise for demonstration.

The typical results are depicted in Fig. 9. The results show that the data points of fringe become more visible after the correction and tend to be more centralized on the fitting curve, which demonstrates the effectiveness of our scheme. It is seen visually that, before the interference fringe recovery, the data points are quite noisy so that an effective fitting is not feasible, but after the correction, it is able to fit the data points. The phase uncertainty σ_{Φ_B} reaches 0.013 rad for data without artificial white noise, while with noise, this value reaches 0.034 rad and 0.019 rad before and after the correction at $T = 0.2$ ms, and the goodness-of-fit is 0.77, 0.31, and 0.59, respectively. And at $T = 0.4$ ms, σ_{Φ_B} reaches 0.019 rad for noise-free case, while this value reaches 0.050 rad and 0.024 rad before and after the correction, with a goodness-of-fit of 0.58, 0.17, and 0.47, respectively. According to Eq. (14), this indicates that the phase noise introduced by δI_{Noise} is effectively compensated.

Although the visibility of the interference fringes is imperfect after the correction, which may be due to the system being unshielded, i.e., the phase noise $\Delta\phi_{\text{others}}$ may be rather large, this transfer function-based fringe recovery mechanism provides an outlook for improving the performance of the multiwave atom interferometer, i.e., we can first use magnetic shielding technology to isolate the majority of magnetic-field fluctuations, which is pointed out in Refs. [26,50,51], and then such a mechanism is applied to compensate for the residual magnetic field fluctuations to enhance the resolution of the interferometer. Hence, this scheme may be beneficial in the magnetic-field-impacted atom interference-based experimental systems and some spinor BEC experiments. The results demonstrate that, even for a metal vacuum chamber which brings difficulty for the calibration of ac magnetic fields to the

position of atoms, the proposed scheme is still effective. In our demonstration, the magnetic field noise is measured through the artificial white current noise. In the case of vibration compensation in an atomic gravimeter where the seismometer measures the vibration near the gravimeter, the counterpart for the multiwave interferometer can be a set of loop antennas measuring the magnetic field noises, which are not near-dc. However, how to calibrate the captured magnetic-field noise from all the directions to the position of the atoms and how to evaluate the impact of the metal chamber regarding the external antennas is far difficult compared to the evaluation of the coefficient k_m . Last but not least, in the experiment, we used a single coil to generate RF fields instead of a pair of Helmholtz coils. The decaying of the Rabi oscillation in Fig. 6(a) is rather slow compared to the demonstrated evolution time. Therefore, the inhomogeneity of the RF fields currently is not the limiting factor. In brief, a more practical design of the magnetic-field noise detector, the evaluation of the inhomogeneity of the RF fields, and T -dependent systematic error can be the concerns for future work.

V. CONCLUSION

In conclusion, the measurement of Ramsey-type interferometer transfer function and the investigation of potential practical applications of the transfer function based on a multiwave atom interferometer in an unshielded, titanium vacuum chamber are proposed and demonstrated. To first calibrate the actual ac magnetic field amplitude at the position of the

atom inside the vacuum chamber, we implement a Raman spectrum-based solution for ac magnetic-field calibration. Then, a magnetically sensitive multiwave Ramsey interferometer is realized based on RF field-coupled Zeeman states. The transfer function of the multiwave atom interferometer to magnetic fields with a low-pass filtering characteristic is subsequently derived by recording the phase variations of the multiwave interferometer under magnetic-field modulation at different frequencies. Taking advantage of this characteristic, we prove, in principle, in the direction of quantization axis, an effective interferometer phase-correction scheme that allows fringe recovery in the presence of artificial white noise. This work will pave the way for practical applications of magnetic-field noise compensation in a magnetically noisy environment.

ACKNOWLEDGMENTS

The authors thank Prof. Xiaochun Duan and Dr. Qin Luo, Lele Chen, and Patrick Cheinet for enlightening discussions. This work is supported by the National Key Research and Development Program of China (Grant No. 2022YFC3003802), the National Natural Science Foundation of China (Grants No. 11922404, No. 11625417, No. 11727809, No. 12004128, and No. 12374464), the Science and Technology Department of Hubei Province, China (Grant No. 2022BAA018), and the Open Fund of Wuhan, Gravitation, and Solid Earth Tides, National Observation and Research Station (Grants No. WHYWZ202211 and No. WHYWZ202104).

-
- [1] A. Peters, K. Y. Chung, and S. Chu, *Metrologia* **38**, 25 (2001).
 - [2] Z.-K. Hu, B.-L. Sun, X.-C. Duan, M.-K. Zhou, L.-L. Chen, S. Zhan, Q.-Z. Zhang, and J. Luo, *Phys. Rev. A* **88**, 043610 (2013).
 - [3] K. S. Hardman, P. J. Everitt, G. D. McDonald, P. Manju, P. B. Wigley, M. A. Sooriyabandara, C. C. N. Kuhn, J. E. Debs, J. D. Close, and N. P. Robins, *Phys. Rev. Lett.* **117**, 138501 (2016).
 - [4] F. Sorrentino, Q. Bodart, L. Cacciapuoti, Y.-H. Lien, M. Prevedelli, G. Rosi, L. Salvi, and G. M. Tino, *Phys. Rev. A* **89**, 023607 (2014).
 - [5] D. Savoie, M. Altorio, B. Fang, L. Sidorenkov, R. Geiger, and A. Landragin, *Sci. Adv.* **4**, eaau7948 (2018).
 - [6] J. B. Fixler, G. Foster, J. McGuirk, and M. Kasevich, *Science* **315**, 74 (2007).
 - [7] G. Rosi, F. Sorrentino, L. Cacciapuoti, M. Prevedelli, and G. Tino, *Nature (London)* **510**, 518 (2014).
 - [8] R. H. Parker, C. Yu, W. Zhong, B. Estey, and H. Müller, *Science* **360**, 191 (2018).
 - [9] L. Morel, Z. Yao, P. Cladé, and S. Guellati-Khélifa, *Nature (London)* **588**, 61 (2020).
 - [10] A. D. Ludlow, M. M. Boyd, J. Ye, E. Peik, and P. O. Schmidt, *Rev. Mod. Phys.* **87**, 637 (2015).
 - [11] S. Beattie, B. Jian, J. Alcock, M. Gertsvolf, R. Hendricks, K. Szymaniec, and K. Gibble, *Metrologia* **57**, 035010 (2020).
 - [12] X.-B. Deng, Y.-Y. Xu, X.-C. Duan, and Z.-K. Hu, *Phys. Rev. Appl.* **15**, 054062 (2021).
 - [13] Y. Eto, H. Ikeda, H. Suzuki, S. Hasegawa, Y. Tomiyama, S. Sekine, M. Sadgrove, and T. Hirano, *Phys. Rev. A* **88**, 031602(R) (2013).
 - [14] Y. Margalit, Z. Zhou, S. Machluf, D. Rohrlich, Y. Japha, and R. Folman, *Science* **349**, 1205 (2015).
 - [15] X.-C. Duan, X.-B. Deng, M.-K. Zhou, K. Zhang, W.-J. Xu, F. Xiong, Y.-Y. Xu, C.-G. Shao, J. Luo, and Z.-K. Hu, *Phys. Rev. Lett.* **117**, 023001 (2016).
 - [16] G. Rosi, G. D'Amico, L. Cacciapuoti, F. Sorrentino, M. Prevedelli, M. Zych, Č. Brukner, and G. Tino, *Nat. Commun.* **8**, 15529 (2017).
 - [17] P. Asenbaum, C. Overstreet, M. Kim, J. Curti, and M. A. Kasevich, *Phys. Rev. Lett.* **125**, 191101 (2020).
 - [18] M. Weitz, T. Heupel, and T. W. Hänsch, *Phys. Rev. Lett.* **77**, 2356 (1996).
 - [19] H. Hinderthür, F. Ruschewitz, H.-J. Lohe, S. Lechte, K. Sengstock, and W. Ertmer, *Phys. Rev. A* **59**, 2216 (1999).
 - [20] J. Petrovic, I. Herrera, P. Lombardi, F. Schaefer, and F. S. Cataliotti, *New J. Phys.* **15**, 043002 (2013).
 - [21] M.-K. Zhou, K. Zhang, X.-C. Duan, Y. Ke, C.-G. Shao, and Z.-K. Hu, *Phys. Rev. A* **93**, 023641 (2016).
 - [22] M. Gustavsson, E. Haller, M. J. Mark, J. G. Danzl, R. Hart, A. J. Daley, and H.-C. Nägerl, *New J. Phys.* **12**, 065029 (2010).
 - [23] W. D. Li, T. He, and A. Smerzi, *Phys. Rev. Lett.* **113**, 023003 (2014).
 - [24] D. Braje, S. DeSavage, C. Adler, J. Davis, and F. Narducci, *J. Mod. Opt.* **61**, 61 (2014).
 - [25] A. A. Wood, L. M. Bennie, A. Duong, M. Jasperse, L. D. Turner, and R. P. Anderson, *Phys. Rev. A* **92**, 053604 (2015).
 - [26] X.-T. Xu, Z.-Y. Wang, R.-H. Jiao, C.-R. Yi, W. Sun, and S. Chen, *Rev. Sci. Instrum.* **90**, 054708 (2019).

- [27] B. Merkel, K. Thirumalai, J. Tarlton, V. Schäfer, C. Ballance, T. Harty, and D. Lucas, *Rev. Sci. Instrum.* **90**, 044702 (2019).
- [28] Z. Meng, L. Wang, W. Han, F. Liu, K. Wen, C. Gao, P. Wang, C. Chin, and J. Zhang, *Nature (London)* **615**, 231 (2023).
- [29] P. Soltan-Panahi, J. Struck, P. Hauke, A. Bick, W. Plenkers, G. Meineke, C. Becker, P. Windpassinger, M. Lewenstein, and K. Sengstock, *Nat. Phys.* **7**, 434 (2011).
- [30] I. Bloch, J. Dalibard, and W. Zwerger, *Rev. Mod. Phys.* **80**, 885 (2008).
- [31] X.-Y. Luo, Y.-Q. Zou, L.-N. Wu, Q. Liu, M.-F. Han, M. K. Tey, and L. You, *Science* **355**, 620 (2017).
- [32] B. Evrard, A. Qu, J. Dalibard, and F. Gerbier, *Science* **373**, 1340 (2021).
- [33] L. Pezze, A. Smerzi, M. K. Oberthaler, R. Schmied, and P. Treutlein, *Rev. Mod. Phys.* **90**, 035005 (2018).
- [34] S. Kotler, N. Akerman, Y. Glickman, A. Keselman, and R. Ozeri, *Nature (London)* **473**, 61 (2011).
- [35] P. Wang, C.-Y. Luan, M. Qiao, M. Um, J. Zhang, Y. Wang, X. Yuan, M. Gu, J. Zhang, and K. Kim, *Nat. Commun.* **12**, 233 (2021).
- [36] J. R. Maze, P. L. Stanwix, J. S. Hodges, S. Hong, J. M. Taylor, P. Cappellaro, L. Jiang, M. Dutt, E. Togan, A. Zibrov *et al.*, *Nature (London)* **455**, 644 (2008).
- [37] A. Laraoui, J. S. Hodges, and C. A. Meriles, *Appl. Phys. Lett.* **97**, 143104 (2010).
- [38] N. V. Vitanov and K.-A. Suominen, *Phys. Rev. A* **56**, R4377(R) (1997).
- [39] W. Yan, X. Ren, M. Zhou, and Z. Hu, *Sensors* **23**, 173 (2022).
- [40] N. F. Ramsey, *Phys. Rev.* **78**, 695 (1950).
- [41] P. Cheinet, B. Canuel, F. P. Dos Santos, A. Gauguier, F. Yver-Leduc, and A. Landragin, *IEEE Trans. Instrum. Meas.* **57**, 1141 (2008).
- [42] J. Le Gouët, T. Mehlstäubler, J. Kim, S. Merlet, A. Clairon, A. Landragin, and F. Pereira Dos Santos, *Appl. Phys. B* **92**, 133 (2008).
- [43] B. Canuel, Étude d'un gyromètre à atomes froids, Ph.D. thesis, Université Paris Sud - Paris XI, 2007.
- [44] J. Bylander, S. Gustavsson, F. Yan, F. Yoshihara, K. Harrabi, G. Fitch, D. G. Cory, Y. Nakamura, J.-S. Tsai, and W. D. Oliver, *Nat. Phys.* **7**, 565 (2011).
- [45] H. Zhang, X. Ren, W. Yan, Y. Cheng, H. Zhou, Z. Gao, Q. Luo, M. Zhou, and Z. Hu, *Opt. Express* **29**, 30007 (2021).
- [46] Q.-Q. Hu, C. Freier, B. Leykauf, V. Schkolnik, J. Yang, M. Krutzik, and A. Peters, *Phys. Rev. A* **96**, 033414 (2017).
- [47] W. Yan, X. Ren, W. Xu, Z. Hu, and M. Zhou, *Front. Phys.* **18**, 52306 (2023).
- [48] Y. Cheng, K. Zhang, L.-L. Chen, T. Zhang, W.-J. Xu, X.-C. Duan, M.-K. Zhou, and Z.-K. Hu, *Phys. Rev. A* **98**, 043611 (2018).
- [49] J. Karki, Active low-pass filter design, Application note, Texas Instruments (2000), www.ti.com/lit/an/sloa049b/sloa049b.pdf.
- [50] H. Dang, A. C. Maloof, and M. V. Romalis, *Appl. Phys. Lett.* **97**, 151110 (2010).
- [51] B. Patton, E. Zhivun, D. C. Hovde, and D. Budker, *Phys. Rev. Lett.* **113**, 013001 (2014).